Article
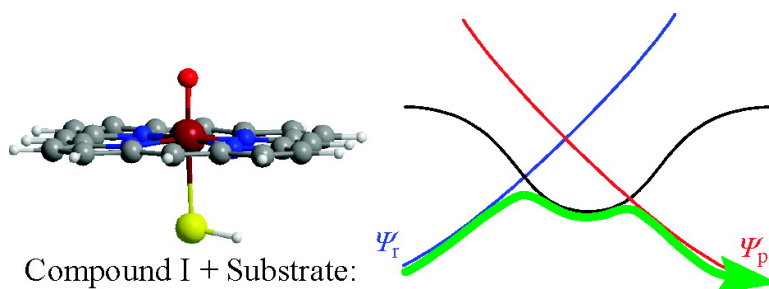
A Valence Bond Modeling of Trends in Hydrogen Abstraction Barriers and Transition States of Hydroxylation Reactions Catalyzed by Cytochrome P450 Enzymes

Sason Shaik, Devesh Kumar, and Sam P. de Visser

Compound I + Substrate: Ψ_r Ψ_p

More About This Article

Additional resources and features associated with this article are available within the HTML version:

- Supporting Information
- Links to the 3 articles that cite this article, as of the time of this article download
- Access to high resolution figures
- Links to articles and content related to this article
- Copyright permission to reproduce figures and/or text from this article

View the Full Text HTML

A Valence Bond Modeling of Trends in Hydrogen Abstraction Barriers and Transition States of Hydroxylation Reactions Catalyzed by Cytochrome P450 Enzymes

Sason Shaik,*,[†] Devesh Kumar,[†,$] and Sam P. de Visser*,[‡]

Institute of Chemistry and the Lise Meitner-Minerva Center for Computational Quantum Chemistry, The Hebrew University of Jerusalem, 91904 Jerusalem, Israel, and The Manchester Interdisciplinary Biocenter and School of Chemical Engineering and Analytical Science, University of Manchester, 131 Princess Street, Manchester M1 7DN, United Kingdom

Received March 17, 2008; E-mail: sason@yfaat.ch.huji.ac.il (S.S.); sam.devisser@manchester.ac.uk (S.P.d.V.)

Abstract: The paper outlines the fundamental factors that govern the mechanisms of alkane hydroxylation by cytochrome P450 and the corresponding barrier heights during the hydrogen abstraction and radical rebound steps of the process. This is done by a combination of density functional theory calculations for 11 alkanes and valence bond (VB) modeling of the results. The energy profiles and transition states for the various steps are reconstructed using VB diagrams (Shaik, S. S. *J. Am. Chem. Soc.* **1981**, *103*, 3692–3701. Shaik, S.; Shurki, A. *Angew. Chem. Int. Ed.* **1999**, *38*, 586–625.) and the DFT barriers are reproduced by the VB model from raw data based on C−H bond energies. The model explains a variety of other features of P450 hydroxylations: (a) the nature of the polar effect during hydrogen abstraction, (b) the difference between the activation mechanisms leading to the Fe^{IV} vs the Fe^{III} electromers, (c) the difference between the gas phase and the enzymatic reaction, and (d) the dependence of the rebound barrier on the spin state. The VB mechanism shows that the active species of the enzyme performs a complex reaction that involves multiple bond making and breakage mechanisms by utilizing *an intermediate VB structure that cuts through the high barrier of the principal transformation between reactants and products, thereby mediating the process at a low energy cost*. The correlations derived in this paper create order and organize the data for a process of a complex and important enzyme. This treatment can be generalized to the reactivity patterns of nonheme systems and synthetic iron−oxo porphyrin reagents.

Introduction

Hydroxylation of nonactivated C−H bonds is one of the most difficult to achieve chemical transformations. Nevertheless, several enzymes that use high valent iron−oxo active species, such as the heme enzymes called cytochromes P450 (P450s) (Scheme 1)[1] and nonheme enzymes, like taurine/α-ketoglutarate dioxygenase (TauD),[2] are known to be efficient catalysts of this reaction. Moreover, many synthetic analogues of P450 and of nonheme enzymes having high-valent metal−oxo complexes have been made and demonstrated to perform C−H hydroxy-lation reactions.[3] This study focuses on P450 with the aim of generating a general theoretical framework that organizes the reactivity patterns of C−H hydroxylation.

Scheme 1 illustrates the active site of the enzyme P450$_{cam}$, which is a bacterial enzyme that regioselectively hydroxylates camphor at the C^5 position.[4,5] It is seen that the iron ion is bound to a protoporphyrin IX macrocycle and linked to the protein backbone via a thiolate linkage of a cysteinate residue (Cys$_{357}$ in P450$_{cam}$). Here and in P450s in general, the binding of the substrate to the active site triggers a series of events that include a reduction of the heme, dioxygen binding, a second reduction step, and finally two protonation events leading to the iron−oxo active species, the so-called compound I (Cpd I).[6] Despite the

[†] The Hebrew University of Jerusalem.
[‡] University of Manchester.
[$] Present Address: Max-Planck-Institut für Kohlenforschung, Kaiser-Wilhelm-Platz 1, D45470 Mülheim an der Ruhr, Germany.

(1) (a) Sono, M.; Roach, M. P.; Coulter, E. D.; Dawson, J. H. *Chem. Rev.* **1996**, *96*, 2841–2887. (b) Guengerich, F. P. *Chem. Res. Toxicol.* **2001**, *14*, 611–650. (c) Ortiz de Montellano, P. R.; De Voss, J. J. *Nat. Prod. Rep.* **2002**, *19*, 477–494. (d) Groves, J. T. *Proc. Natl. Acad. Sci. U.S.A.* **2003**, *100*, 3569–3574. (e) *Cytochrome P450: Structure, Mechanism and Biochemistry*, 3rd ed.; Ortiz de Montellano, P. R., Ed.; Kluwer Publishers/Plenum Press: New York, 2005.

(2) (a) Ryle, M. J.; Hausinger, R. P. *Curr. Opin. Chem. Biol.* **2002**, *6*, 193–201. (b) Costas, M.; Mehn, M. P.; Jensen, M. P.; Que, L., Jr *Chem. Rev.* **2004**, *104*, 939–986. (c) Abu-Omar, M. M.; Loaiza, A.; Hontzeas, N. *Chem. Rev.* **2005**, *105*, 2227–2252. (d) Krebs, C.; Fujimori, D. G.; Walsh, C. T.; Bollinger, J. M., Jr *Acc. Chem. Res.* **2007**, *40*, 484–492.

(3) See, for example: (a) Groves, J. T. *J. Inorg. Biochem.* **2006**, *100*, 434–447. (b) Rohde, J.-U.; In, J.-H.; Lim, M. H.; Brennessel, W. W.; Bukowski, M. R.; Stubna, A.; Münck, E.; Nam, W.; Que, L., Jr *Science* **2003**, *299*, 1037–1039. (c) Lim, M. H.; Rohde, J.-U.; Stubna, A.; Bukowski, M. R.; Costas, M.; Ho, R. Y. N.; Münck, E.; Nam, W.; Que, L., Jr *Proc. Natl. Acad. Sci. U.S.A.* **2003**, *100*, 3665–3670.

(4) (a) Schlichting, I.; Berendzen, J.; Chu, K.; Stock, A. M.; Maves, S. A.; Benson, D. E.; Sweet, R. M.; Ringe, D.; Petsko, G. A.; Sligar, S. G. *Science* **2000**, *287*, 1615–1622. (b) Davydov, R.; Makris, T. M.; Kofman, V.; Werst, D. E.; Sligar, S. G.; Hoffman, B. M. *J. Am. Chem. Soc.* **2001**, *123*, 1403–1415.

(5) Poulos, T. L.; Finzel, B. C.; Howard, A. J. *J. Mol. Biol.* **1987**, *195*, 687–700.

(6) Meunier, B.; de Visser, S. P.; Shaik, S. *Chem. Rev.* **2004**, *104*, 3947–3980.

Scheme 1. An Illustration of the Iron−Oxo Active Species of Cytochrome P450$_{cam}$ That Regioselectively Hydroxylates the C^5−H$_{exo}$ Bond of Camphor (taken from PDB file 1DZ9)[4a]
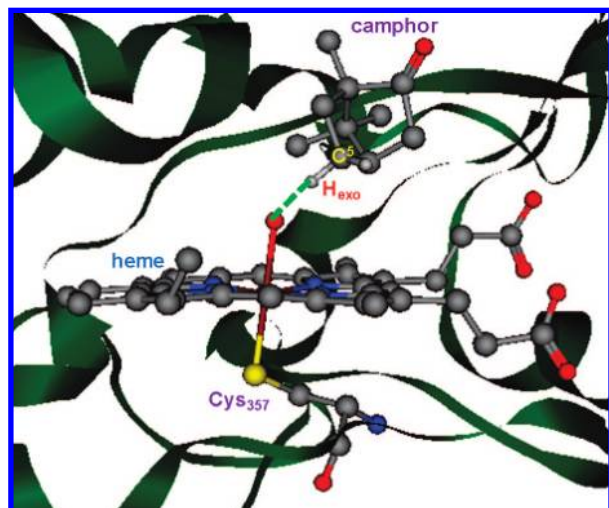
Scheme 2. The Groves Rebound Mechanism of Alkane (Alk−H) Hydroxylation by Iron−Oxo Species
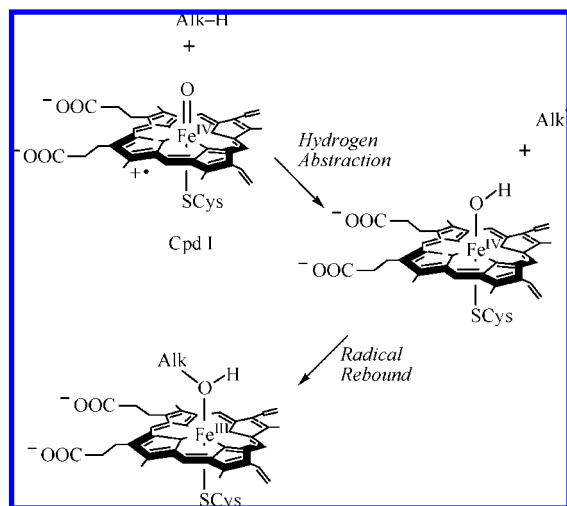
elusiveness of Cpd I in the working cycle of the enzyme, its presence can be inferred in a variety of ways, and it is generally assumed to be the species that performs the hydroxylation.[4b,7]

The net reaction between Cpd I and an alkane (AlkH) involves, in addition to the C−H bond activation, lowering of the oxidation state of the heme by two oxidation equivalents. Thus, as shown in Scheme 2, Cpd I, labeled Por$^{+\bullet}$Fe^{IV}=O with Por = protoporphyrin IX, changes its oxidation state during the reaction to PorFe^{III}O(H)Alk in the products. As such, the metal and the protoporphyrin groups are both reduced by one oxidation equivalent. This reduction is common to other oxidation reactions, e.g., in the nonheme dioxygenases, where the oxidation state changes from Fe^{IV} to Fe^{II}.[2b] The question is, how is this interplay of bond activation and "redox" property, inherent to the net reaction, being expressed in the reactivity patterns of the hydroxylation reactions?

Recently there have appeared a number of publications that demonstrated computationally in P450s,[8] experimentally in synthetic heme,[9] and both experimentally and computationally in nonheme complexes[10] and in other metal−oxo reagents[11] that the reactivity ordering follows the bond dissociation energy (BDE) of the C−H bond in the alkane as well as the BDE of the forming O−H bond of the metal−oxo reagent.[8a,11] The origin of these correlations is usually interpreted by invoking the Brønsted−Bell−Evans−Polanyi (BBEP) principle,[11a,12] whereby one might expect that the barrier would decrease as the hydrogen-abstraction reaction becomes more exothermic (exoergic). But we must recall that even in the first step of the reaction the iron−oxo reagent undergoes a redox reaction and its oxidation state is lowered by one oxidation equivalent (see Scheme 2). Indeed, at least in the case of nonheme iron−oxo reagents, the reactivity of the series of alkanes correlates nicely not only with the BDE$_{C−H}$,[10a] but also with the corresponding ionization potential (IP) of the alkane, IP(AlkH).[13] Similar dual correlations exist in P450 hydroxylation, where a good correlation was reported between the reaction rate and the redox properties of the alkanes, such as in the *N,N*-dimethylaniline series.[14] It is arguable that this "dual" correlation exists because in some series of alkanes the two molecular properties correlate with each other. Still, this raises a few questions. One question concerns the causality relationship: Does the correction with BDE$_{C−H}$ or with IP(AlkH) imply a causal relationship, or are these just useful correlations with no causal implication? And, second, why does one often get these extended correlations with BDE$_{C−H}$ in such oxidative reactions? Another set of questions concerns the mechanism, beautifully termed by Groves as the rebound mechanism:[15] why is it stepwise and not concerted? What are the factors that control the final alcohol formation step?

A clear answer to these questions can emerge from a quantum chemical modeling of the reaction mechanism and barrier formation in each mechanistic step. This is the main goal of the present paper, which seeks to pattern the reactivity trends by focusing on P450 hydroxylation as a general paradigm for these reactions. As such, we approach the problem in a two-pronged manner: We first perform an extended series of calculations for P450 C−H activation of alkanes, as in Scheme

(7) Perera, R.; Jin, S.; Sono, M.; Dawson, J. H. Cytochrome P450-Catalyzed Hydroxylations and Epoxidations. In *Metal Ions in Life Sciences: The Ubiquitous Roles of Cytochrome P450 Proteins*; Sigel, A., Sigel, H., Sigel, R. K. O., Eds.; Wiley: New York, 2007; Vol. 3, Chapter 11, p 319.

(8) (a) Korzekwa, K. R.; Jones, J. P.; Gillette, J. R. *J. Am. Chem. Soc.* **1990**, *112*, 7042–7046. (b) de Visser, S. P.; Kumar, D.; Cohen, S.; Shacham, R.; Shaik, S. *J. Am. Chem. Soc.* **2004**, *126*, 8362–8363. (c) Olsen, L.; Rydberg, P.; Rod, T. H.; Ryde, U. *J. Med. Chem.* **2006**, *49*, 6489–6499. (d) Kamachi, T.; Yoshizawa, K. *J. Am. Chem. Soc.* **2003**, *125*, 4652–4661.

(9) Jin, N.; Bourassa, J. L.; Tizio, S. C.; Groves, J. T. *Angew. Chem., Int. Ed.* **2000**, *39*, 3849–3851.

(10) (a) Kaizer, J.; Klinker, E. J.; Oh, N. Y.; Rohde, J.-U.; Song, W. J.; Stubna, A.; Kim, J.; Münck, E.; Nam, W.; Que, L., Jr. *J. Am. Chem. Soc.* **2004**, *126*, 472–473. (b) Hirao, H.; Kumar, D.; Que, L., Jr.; Shaik, S. *J. Am. Chem. Soc.* **2006**, *128*, 8590–8606.

(11) (a) Mayer, J. M. *Acc. Chem. Res.* **1998**, *31*, 441–450. (b) Mayer, J. M. In *Biomimetic Oxidations Catalyzed by Transition Metal Complexes*; Meunier, B., Ed.; Imperial College Press: London, 1999; 1–43.

(12) (a) Bell, R. P. *Proc. R. Soc. London Ser. A* **1936**, *154*, 414–421. (b) Evans, M. G.; Polanyi, M. *Trans. Faraday Soc.* **1938**, *34*, 11–24. (c) See comments: Pross, A.; Shaik, S. S. *Nouv. J. Chim.* **1989**, *13*, 427–433.

(13) Sydora, O. L.; Goldsmith, J. I.; Vaid, T. P.; Miller, A. E.; Wolczanski, P. T.; Abruña, H. D. *Polyhedron* **2004**, *23*, 2841–2856.

(14) (a) Okazaki, O.; Guengerich, F. P. *J. Biol. Chem.* **1993**, *268*, 1546–1552. (b) Wang, Y.; Kumar, D.; Yang, C.; Han, L.; Shaik, S. *J. Phys. Chem. B* **2007**, *111*, 7700–7710. (c) Li, C.; Wu, W.; Kumar, D.; Shaik, S. *J. Am. Chem. Soc.* **2006**, *128*, 394–395.

(15) Groves, J. T.; McClusky, G. A. *J. Am. Chem. Soc.* **1976**, *98*, 859–861.
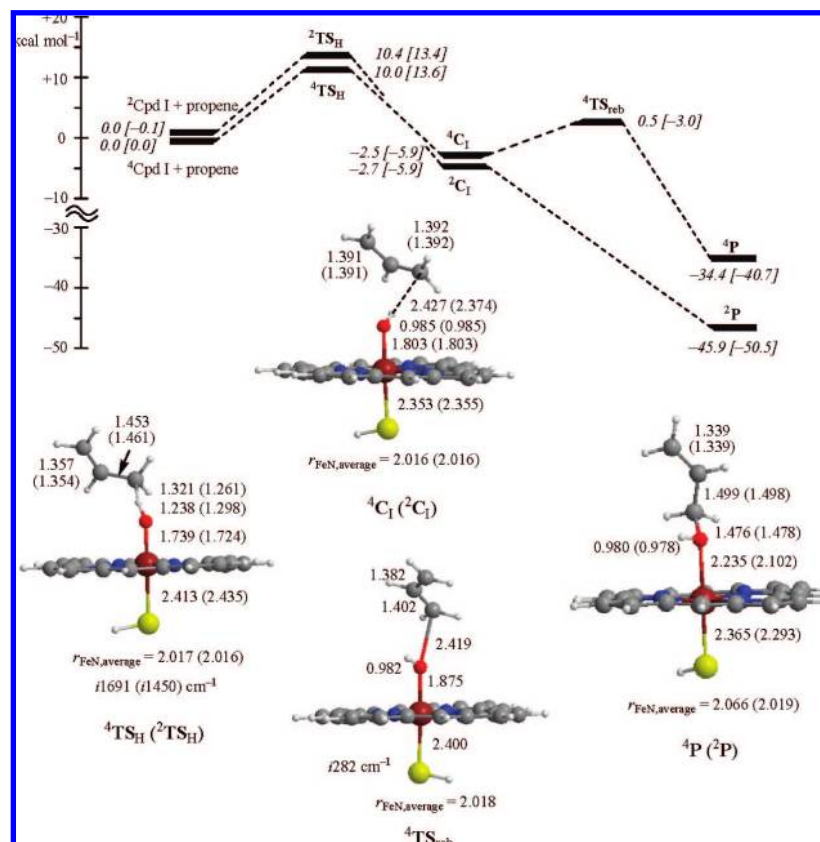
Figure 1. Potential energy profiles and optimized geometries of the critical points for the allylic hydroxylation of propene by ^{4,2}Cpd I. All energies ($\Delta(E+\text{ZPE})$) are in kcal mol^{-1} relative to isolated ^{4}Cpd I and propene reactants with energies calculated with basis set B1 (B2 data in square brackets). Bond lengths are in Å and the value of the imaginary frequency of the transition state is in cm^{-1}.

2, where Alk–H corresponds to methane (**1**),[16] ethane (**2**),[8b] propane (**3**),[8b] propene (**4**),[17] *trans*-methylphenylcyclopropane (**5**),[18] *trans*-isopropylphenylcyclopropane (**6**),[18] *N,N*-dimethyl-aniline (**7**),[14b] toluene (**8**),[19] phenylethane (**9**), and camphor (**10**). *N,N*-Dimethylaniline belongs to a series whose reactivity does not follow the trend in BDE.[14b,c] Subsequently, we use valence bond theory[20] to model computational results and elucidate the origins of the various barriers and transition state (TS) structures.

Methods

Software. In order to calculate a series of hydrogen abstraction barriers as catalyzed by a Cpd I model of P450 enzymes, with small nonsystematic errors, we decided to reoptimize all transition states that appeared in our previous set of calculations.[8b,14b,16–19] That way we are able to create a data set of which all systems are calculated using the same methods, procedures, and basis sets. This should remove any nonsystematic errors from the calculations and enable us to describe trends of barrier heights and establish a VB correlation for the series. All the calculations were previously[8b] done using the Jaguar 4.2 program package[21] for geometry

optimization and Gaussian 98[22] for frequency calculations. Since we have noticed that occasionally Jaguar and Gaussian yield slightly different transition state structures,[23] it was deemed necessary to repeat all the geometry optimizations and frequencies with Gaussian 03,[24] which possesses a robust geometry optimization routine. Although, small differences in transition state geometries, imaginary frequencies, and energies between the Jaguar and Gaussian 03 data sets (see Supporting Information for details) were found, the reaction barriers themselves did not change significantly, so all previous conclusions based on the Jaguar optimizations remain valid. The changes in geometries and frequencies are not large but nevertheless affected the zero point energy (ZPE) corrections and, as a result, introduced significant error bars on kinetic isotope effect values for the two spin state processes (see Table S1 in the Supporting Information). However, the calculated energy differences ranged between 0 and 1.5 kcal mol^{-1} and did not affect the correlations that are discussed in the text. Both barrier data sets correlated perfectly with each other (Figure S12 of the Supporting Information) and exhibit similar correlations with BDEs. Therefore, we will focus on the newly generated Gaussian 03 data in this paper, while all other data is relegated to the Supporting Information.

Functional and Basis Sets. All the calculations presented here were performed using the unrestricted hybrid density functional method UB3LYP.[25] Geometry optimizations (without constraints) followed by analytical frequency calculations were performed in Gaussian 03 with an LACVP basis set on iron and a 6-31G basis

(16) Ogliaro, F.; Harris, N.; Cohen, S.; Filatov, M.; de Visser, S. P.; Shaik, S. *J. Am. Chem. Soc.* **2000**, *122*, 8977–8989.

(17) (a) de Visser, S. P.; Ogliaro, F.; Sharma, P. K.; Shaik, S. *Angew. Chem. Int. Ed* **2002**, *41*, 1947–1951. (b) de Visser, S. P.; Ogliaro, F.; Sharma, P. K.; Shaik, S. *J. Am. Chem. Soc.* **2002**, *124*, 11809–11826.

(18) (a) Kumar, D.; de Visser, S. P.; Shaik, S. *J. Am. Chem. Soc.* **2003**, *125*, 13024–13025. (b) Kumar, D.; de Visser, S. P.; Sharma, P. K.; Cohen, S.; Shaik, S. *J. Am. Chem. Soc.* **2004**, *126*, 1907–1920.

(19) Hazan, C.; Kumar, D.; de Visser, S. P.; Shaik, S. *Eur. J. Inorg. Chem.* **2007**, 2966–2974.

(20) (a) Shaik, S. S. *J. Am. Chem. Soc.* **1981**, *103*, 3692–3701. (b) Shaik, S.; Shurki, A. *Angew. Chem., Int. Ed.* **1999**, *38*, 586–625.
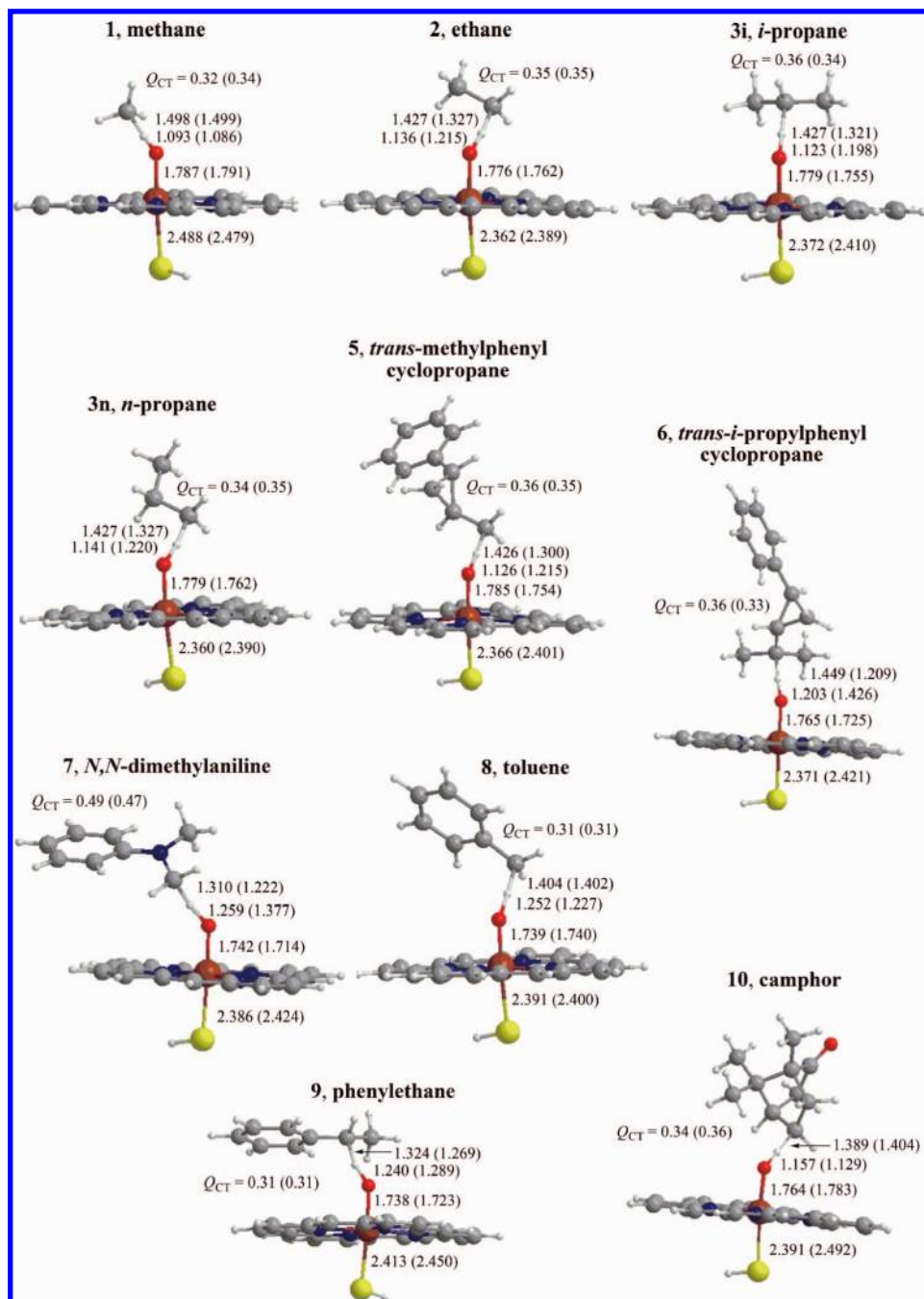
(21) *Jaguar 4.2*; Schrödinger, LLC: Portland, OR, 2000.

(22) Frisch, M. J. *Gaussian 98*; Gaussian: Wallingford, CT, 1998.

(23) (a) Sharma, P. K.; de Visser, S. P.; Shaik, S. *J. Am. Chem. Soc.* **2003**, *125*, 8698–8699. (b) de Visser, S. P. *J. Am. Chem. Soc.* **2006**, *128*, 9813–9824. (c) Godfrey, E.; Porro, C. P.; de Visser, S. P. *J. Phys. Chem. A* **2008**, *112*, 2464–2468.

(24) Frisch, M. J. *Gaussian 03*; Gaussian: Wallingford, CT, 2003.

Figure 2. Key geometric features of H-abstraction transition states obtained at the UB3LYP/B1 level for **1–3i** and **5–10**. The data is displayed respectively as ^4TS_H (^2TS_H) with bond lengths in Å. The Q_{CT} data correspond to the amounts of charge transferred from the alkane to Cpd I in the transition state calculated at the NBO/B3LYP/B2 level.

set on the rest of the atoms (basis set B1).[26,27] Subsequent, single-point calculations were done on the optimized geometries in Jaguar 7.0 using a triple-ζ quality LACV3P+ basis set on iron and 6-311+G* on the rest of the atoms (basis set B2), which were done to correct the energies, but essentially gave the same trends as the double-ζ basis set.[28] All ZPE values reported in this work are taken

from the UB3LYP/B1 frequency calculations. These methods and procedures were shown to reproduce experimental free energies of activation and kinetic isotope effects.[29]

Models and Systems. To model Cpd I of P450, the species was truncated as an iron–oxo porphine with HS$^-$ as axial ligand, since it was shown to be a good representation of the actual cysteinate

(25) (a) Becke, A. D. *J. Chem. Phys.* **1992**, *96*, 2155–2160. (b) Becke, A. D. *J. Chem. Phys.* **1992**, *97*, 9173–9177. (c) Becke, A. D. *J. Chem. Phys.* **1993**, *98*, 5648–5652. (d) Lee, C.; Yang, W.; Parr, R. G. *Phys. Rev. B* **1988**, *37*, 785–789.
(26) Hay, P. J.; Wadt, W. R. *J. Chem. Phys.* **1985**, *82*, 299–308.
(27) Hehre, W. J.; Ditchfield, R.; Pople, J. A. *J. Chem. Phys.* **1972**, *56*, 2257–2261.
(28) Jaguar 7.0, Schrödinger, LLC, New York, NY, 2007.

(29) de Visser, S. P.; Oh, K.; Han, A.-R.; Nam, W. *Inorg. Chem.* **2007**, *46*, 4632–4641.
(30) (a) Ogliaro, F.; de Visser, S. P.; Cohen, S.; Kaneti, J.; Shaik, S. *ChemBioChem.* **2001**, *7*, 848–851. (b) Schöneboom, J. C.; Lin, H.; Reuter, N.; Thiel, W.; Cohen, S.; Ogliaro, F.; Shaik, S. *J. Am. Chem. Soc.* **2002**, *124*, 8142–8151. (c) de Visser, S. P.; Shaik, S.; Sharma, P. K.; Kumar, D.; Thiel, W. *J. Am. Chem. Soc.* **2003**, *125*, 15779–15788.
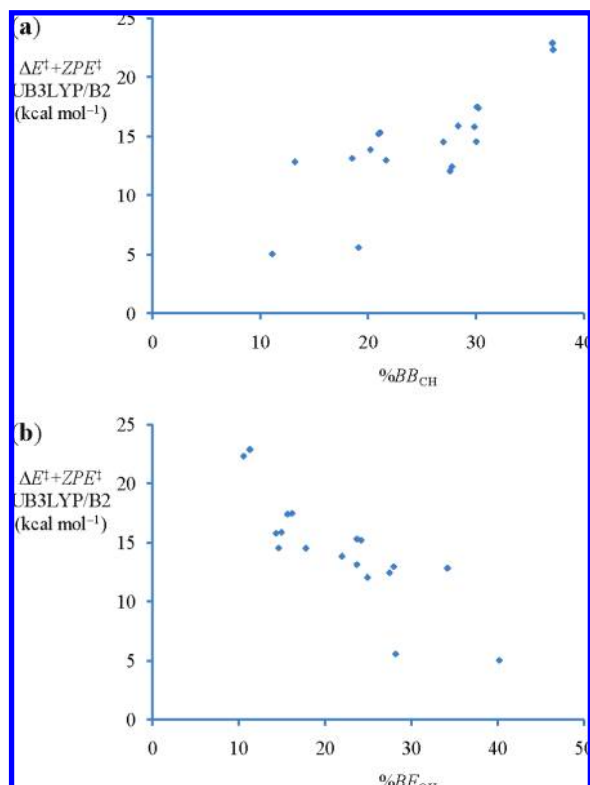
Figure 3. Plots of the barriers for the C—H bond activation of **1**–**10**, against the percentage of bond breaking, %BB_{CH} (a), and of bond formation, %BF_{OH} (b).

ligand.[30] Typically, Cpd I is a two-state reagent with close-lying doublet and quartet ground states (^{4,2}Cpd I), which react via different pathways with substrates.[31] Generally, the doublet (low spin, LS) spin surface gives an effectively concerted reaction path, whereas the quartet (high spin, HS) spin surface is stepwise. Thus ^{4,2}Cpd I reacts via two-state reactivity (TSR) with substrates with different HS and LS reaction barriers.[31,32] As indicated in the Introduction, the hydrogen-abstraction transition states for the reaction with ^{4,2}Cpd I were calculated for the following substrates: methane (**1**), ethane (**2**), propane (**3**), propene (**4**), *trans*-methylphenylcyclopropane (**5**), *trans*-isopropylphenylcyclopropane (**6**), *N,N*-dimethylaniline (**7**), toluene (**8**), phenylethane (**9**), and camphor (**10**). The set of substrates covers a large range of hydrogen-abstraction barriers with a large variation in the C—H bond strengths that are activated in the process. In the case of propane, both hydrogen abstraction from the primary and secondary carbon atoms were studied, which we labeled **3n** and **3i**, respectively. In our previous work,[8b] we reported the phenylethane hydroxylation from the primary carbon atom, but here we focused on the realistic process of C—H activation in the benzylic position. In total, this set generated 22 hydrogen abstraction reactions that are calculated with the same models, same methods, same basis sets, and the same software packages. This should remove many systematic errors and enable us to find trends in the data set and to model it by use of valence bond diagrams.[20b] Charges were obtained with the natural bond orbital analysis (NBO) program[33] at UB3LYP/B1 in Gaussian 03 and at UB3LYP/B2 in Jaguar 7.0. To test the effect of the environment on the barrier heights, single-point calculations using

the UB3LYP/B2 method were performed with Jaguar using a solvent with a dielectric constant of $\varepsilon = 5.7$ and a probe radius of 2.72 Å.

Auxiliary Data. The bond dissociation energies (BDE_{CH} and BDE_{OH}) of the aliphatic C—H bond of the substrates (Alk—H) and of the O—H bond in the iron—hydroxo complexes (see Figure 1) were calculated and defined from the energy difference of the following reactions:

$$Alk-H \rightarrow Alk\bullet + H\bullet + BDE_{CH} \quad (1)$$

$$PorFeO-H \rightarrow PorFe=O(Cpd\ I) + H\bullet + BDE_{OH} \quad (2)$$

For completeness and consistency with the hydrogen abstraction barriers, we recalculated these BDE values using Gaussian 03 with basis set B1 followed by a single-point calculation with basis set B2 so that all data discussed here is calculated using the same methods and procedures. In our previous study, we showed that BDEs calculated with Gaussian 98 and the B3LYP/6-31G (B1) or B3LYP/6-311++G** (B3) basis sets give similar correlations with reaction barriers.[8b] BDE_{CH} is calculated for the isolated reactants while BDE_{OH} is for the substrate free reaction in eq 2.

From the geometry of the Alk residue in the substrate and in the Alk• radical, we estimated the reorganization energy of the radical ($RE_{Alk\bullet}$) as the energy difference of the Alk• rest group in the free substrate and in the fully relaxed geometry of the Alk• radical.[34] The combination of BDE_{CH} and $RE_{Alk\bullet}$ in eq 3 defines the bond strength (D_{CH}), which is a more faithful measure of the interaction strength between the bonded Alk and H moieties in the alkane:[8b]

$$D_{CH} = BDE_{CH} + RE_{Alk} \quad (3)$$

All the data generated in this study are shown in the Supporting Information. For space economy, the following sections will focus on the key data only.

Results

Energy Profiles. Figure 1 shows an example of a typical two-state reactivity (TSR) mechanism of an alkane hydroxylation reaction by Cpd I,[32] in this case for the C—H activation of the methyl group of propene. All the substrates studied follow essentially the same reaction mechanism as displayed in Figure 1 and only the relative energies vary. The energetics of the reaction are similar to those obtained previously with slightly different methods and techniques.[17] The initial step involves a hydrogen abstraction by ^{4,2}Cpd I from the substrate via barrier ^{4,2}TS$_H$ leading to an intermediate (^{4,2}C$_I$) consisting of an iron—hydroxo group and a nearby allyl radical. Since Cpd I has a degenerate quartet and doublet ground state,[31,32] there are reaction barriers on both spin surfaces, with the ^{4}TS$_H$ barrier being slightly higher in energy than the one passing via ^{2}TS$_H$ (13.6 vs 13.4 kcal mol^{-1}, using basis set B2). Within the intermediate complex, the radical rebounds onto the hydroxo group via ^{4,2}TS$_{reb}$ to form the ferric—propenol products (^{4,2}P). On the HS surface, a small but significant barrier ($\Delta E^{\ddagger} + ZPE^{\ddagger}$ for ^{4}TS$_{reb}$ is 2.9 kcal mol^{-1}, with basis set B2) separates intermediates from products, while the LS pathway is essentially barrier free. Thus, the HS intermediate (^{4}C$_I$) will have a finite lifetime in which, for instance, rearrangement leading to side reactions can take place.[35] We recall from previous publications that the iron—hydroxo complexes in the ^{4,2}C$_I$ intermediates come in two electromeric varieties: ^{4,2}Por$^+$•Fe^{III}OH and ^{4,2}Por-

(31) Shaik, S.; de Visser, S. P.; Ogliaro, F.; Schwarz, H.; Schröder, D. *Curr. Opin. Chem. Biol.* **2002**, *6*, 556–567.

(32) Shaik, S.; Kumar, D.; de Visser, S. P.; Altun, A.; Thiel, W. *Chem. Rev.* **2005**, *105*, 2279–2328.

(33) Reed, A. E.; Curtiss, L. A.; Weinhold, F. *Chem. Rev.* **1988**, *88*, 899–926.

(34) Bernardi, F.; Cherry, W.; Shaik, S.; Epiotis, N. D. *J. Am. Chem. Soc.* **1978**, *100*, 1352–1356.

(35) (a) de Visser, S. P.; Ogliaro, F.; Shaik, S. *Angew. Chem., Int. Ed.* **2001**, *40*, 2871–2874. (b) de Visser, S. P.; Kumar, D.; Shaik, S. *J. Inorg. Biochem.* **2004**, *98*, 1183–1193. (c) Kumar, D.; de Visser, S. P.; Shaik, S. *Chem. Eur. J.* **2005**, *11*, 2825–2835.

Table 1. Barriers, $\Delta E^{\ddagger}$, and $\Delta E^{\ddagger} + ZPE^{\ddagger}$ relative to separated reactants, ^{4,2}Cpd I + Alk-H[a,b]

		TS$_H$(B1)		TS$_H$(B2)	
		$\Delta E^{\ddagger}$	$\Delta E^{\ddagger} + ZPE^{\ddagger}$	$\Delta E^{\ddagger}$	$\Delta E^{\ddagger} + ZPE^{\ddagger}$
		High-Spin (Quartet) Data			
1	methane	26.77	22.81	26.87	22.91
2	ethane	21.32	17.71	21.02	17.41
3i	*i*-propane	19.05	15.39	19.46	15.80
3n	*n*-propane	21.47	17.84	21.12	17.48
4	propene	14.68	11.70	15.93	12.95
5	*trans*-methylphenylcyclopropane	18.28	14.73	18.09	14.53
6	*trans*-isopropylphenylcyclopropane	16.03	12.46	17.03	13.46
7	*N,N*-dimethylaniline	7.66	5.04	8.17	5.54
8	toluene	14.81	11.79	15.45	12.43
9	phenylethane	14.57	11.19	15.93	12.55
10	camphor	17.96	14.21	18.27	14.51
		Low-Spin (Doublet) Data			
1	methane	25.87	22.24	25.97	22.34
2	ethane	20.23	16.65	18.88	15.30
3i	*i*-propane	17.68	14.17	17.36	13.85
3n	*n*-propane	20.36	16.70	18.85	15.19
4	propene	15.15	12.13	15.85	12.82
5	*trans*-methylphenylcyclopropane	17.31	13.90	16.54	13.13
6	*trans*-isopropylphenylcyclopropane	15.05	11.64	15.68	12.27
7	*N,N*-dimethylaniline	6.65	4.53	7.11	4.99
8	toluene	14.78	11.73	15.10	12.05
9	phenylethane	14.21	10.69	15.00	11.47
10	camphor	18.39	14.02	20.25	15.88

[a] All energies are in kcal mol^{-1}. [b] Data obtained after full optimization and frequency in Gaussian 03 using UB3LYP/B1 and after additional single-point UB3LYP/B2 calculation in Jaguar 7.0.

Table 2. Calculated BDE$_{CH}$, BDE$_{OH}$, and RE$_{Alk\bullet}$ Data of All the Species Mentioned in the Text[a]

	BDE$_{CH}$				RE$_{Alk\bullet}$	
	B1		B2		ΔE	
	ΔE	$\Delta E + ZPE$	ΔE	$\Delta E + ZPE$	B1	B2
methane	112.45	102.77	111.29	101.62	−7.42	−6.79
ethane	107.51	97.70	106.67	96.87	−7.45	−7.00
i-propane	103.39	93.55	102.87	93.03	−7.56	−7.21
n-propane	107.98	98.37	107.09	97.49	−7.23	−6.87
propene	91.48	82.89	91.39	82.80	−17.69	−16.69
trans-methylphenylcyclopropane	103.66	94.32	102.96	93.62	−9.00	−8.30
trans-isopropylphenylcyclopropane	95.92	86.56	95.95	86.60	−9.04	−8.60
N,N-dimethylaniline	95.72	86.99	94.81	86.08	−8.14	−7.94
toluene	94.45	86.08	94.16	85.80	−13.15	−12.27
phenylethane	91.30	82.44	91.31	82.45	−19.32	−18.38
camphor	104.08	94.58	103.39	93.89	−7.90	−7.61
FeOH	88.59	81.81	95.69	88.91		

[a] All data are in kcal mol^{-1} and calculated with basis set B1 or B2. ZPE data calculated with basis set B1.

Fe^{IV}OH.[36] The latter are lower in energy than the former in the gas phase, while in the protein both state varieties are very close in energy. The same patterns apply to the ^{4,2}TS$_H$ and ^{4}TS$_{reb}$ species.[32] We shall address the processes for the two electromers and delineate their similarities and differences below.

The rate-determining step in most systems studied for both HS and LS surfaces is the initial hydrogen abstraction step via ^{4,2}TS$_H$. The hydrogen abstraction transition states (^{4,2}TS$_H$) for all systems studied are characterized by an almost linear O−H−C angle. While we shall attempt to model the entire mechanism using VB diagrams,[20] a major focus of this paper is going to be the hydrogen-abstraction step. The rebound step has been discussed in great detail elsewhere[37] and will receive here somewhat less attention.

Structures and Trends in the Transition States for H-Abstraction. The key geometric features of the H-abstraction transition states, for the substrates **1**−**3i** and **5**−**10** are depicted

(36) de Visser, S. P.; Ogliaro, F.; Harris, N.; Shaik, S. *J. Am. Chem. Soc.* **2001**, *123*, 3037–3047.

(37) (a) Shaik, S.; Cohen, S.; de Visser, S. P.; Ogliaro, F.; Sharma, P. K. *Eur. J. Inorg. Chem.* **2004**, 207–226. (b) Shaik, S.; Hirao, H.; Kumar, D. *Nat. Prod. Rep.* **2007**, *24*, 533–552.
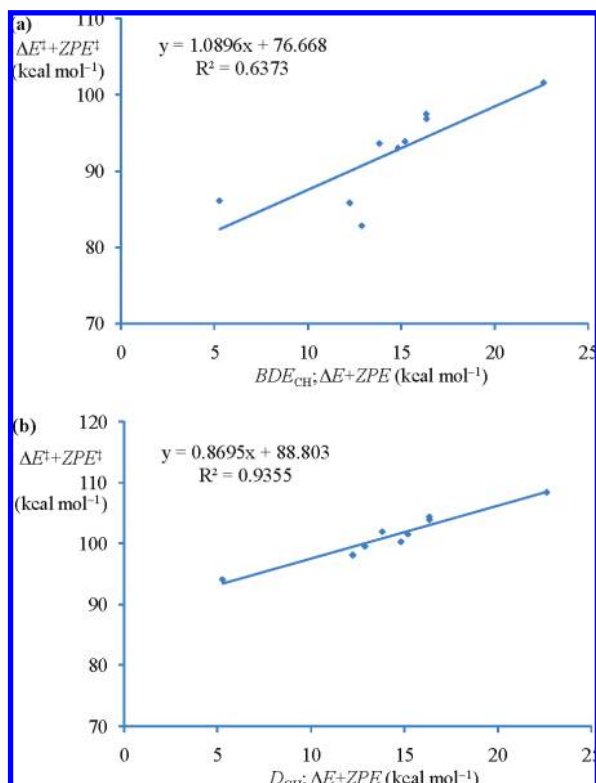
Figure 4. (a) A plot of the average barriers $\Delta E^{\ddagger} + ZPE^{\ddagger}$ (B2) for the quartet and doublet H-abstraction steps vs BDE_{CH} (B2). (b) A plot of the average barriers $\Delta E^{\ddagger} + ZPE^{\ddagger}$ for the quartet and doublet H-abstraction steps vs D_{CH} (defined by eq 3) as calculated with basis set B2.

in Figure 2 (for **4**, see Figure 1), where the data is given in respective order for ^4TS_H (^2TS_H). Also indicated in the figure are the amounts of charge transfer, Q_{CT}, from the substrate to Cpd I, using the NBO/B2 method for charge partition. It is seen that, generally, the quartet spin state structures involve a greater extent of C–H bond cleavage, in accord with the general trend discussed above with reference to Figure 1. The O–H bond is quite short in all the transition states. Another common feature is the O–H–C angle, which is close to 180° in all the computed species. The charge distribution shows that in the transition state the alkane transfers approximately 0.31–0.36 e⁻ (NBO/B2) to Cpd I, with the exception of **7** (*N,N*-dimethylaniline), where the Q_{CT} corresponds to 0.49 (0.47) for ^4TS_H (^2TS_H), respectively. This charge transfer is in accord with the notion from the oxidation state formalism that the process involves also a change in the oxidation state of Cpd I. In this respect, the spin density distribution (Table S4 in the Supporting Information) shows that all the transition states (with the exception of **1**) are more of the Fe^{IV} type rather than of the Por$^{\bullet+}$Fe^{III} type. We recall that in the protein the latter electromers are more stable.[38]

Figure 3 depicts the barriers plotted against the percentages of bond breaking (%BB) and bond formation (%BF) for all transition states calculated here. Thus, the percentage of bond breaking of the C–H bond (%BB$_{CH}$) is defined as the elongation of the C–H distance in the transition state relative to the one in the reactants. Similarly, the percentage of bond formation of

(38) (a) Schöneboom, J. C.; Cohen, S.; Lin, H.; Shaik, S.; Thiel, W. *J. Am. Chem. Soc.* **2004**, *126*, 4017–4034. (b) Altun, A.; Shaik, S.; Thiel, W. *J. Am. Chem. Soc.* **2007**, *129*, 8978–8987. (c) Harvey, J. N.; Bathelt, C. M.; Mulholland, A. J. *J. Comput. Chem.* **2006**, *27*, 1352–1362.

the O–H bond (%BF$_{OH}$) is the distance in the transition state relative to that in the iron–hydroxo intermediate. As can be seen from Figure 3, the %BB$_{CH}$ and %BF$_{OH}$ are generally correlated with the height of the barrier for the C–H bond activation. In particular, the C–H bond elongation in the transition state is longer for the transition states with higher barriers, i.e. the structures are of product-like geometry. By contrast, when the barrier is low, the respective transition states show reactant-type geometries with short C–H and long O–H distances. It appears, therefore, that the nature of all these transition states is similar and that a common electronic effect determines the height of the hydrogen abstraction barrier. Later in this paper we will explain these functions through VB modeling of the barriers.

Reaction Barriers and Bond Dissociation Energies during H-Abstraction. The barriers for the H-abstraction processes for all the systems are collected in Table 1 for the UB3LYP/B1 and UB3LYP/B2 results. These barriers are close to the ones computed before with slightly different methods and basis sets and follow similar trends.[8b,17–19] The Supporting Information provides detailed comparisons of the Jaguar and Gaussian 03 optimized structures, but since the barrier heights are similar, we focus only on the trends of the barriers here. Furthermore, test calculations using the effect of a bulk polarity showed that the barriers are influenced to a similar extent, with a standard deviation of ±1.2 kcal mol⁻¹. Therefore, the trends as obtained from the gas-phase calculations can be extrapolated to situations in the protein or other environments.

Table 2 shows the corresponding BDE$_{CH}$ (B1 and B2) values and the reorganization energies RE$_{Alk}$ of the radical species. The last entry in Table 2 gives the corresponding BDE$_{OH}$ datum for the iron–hydroxo species. Using these BDE$_{CH}$ data and the BDE$_{OH}$ values, one can calculate the thermodynamic driving forces of the processes.

BBEP Correlations of Barriers with Bond Dissociation Energies. The correlation of activation barriers (logarithms of reaction rates) with BDEs derives from the Brønsted–Bell–Evans–Polanyi (BBEP) principle,[12] which relates the barrier to the reaction exothermicity (exoergicity). The reaction energy (ΔE in energy or free energy units) for the H-abstraction step in Figure 1, is given by eq 4,

$$\Delta E = BDE_{CH} - BDE_{OH} \qquad (4)$$

in terms of the bond dissociation energy difference of the C–H bond undergoing abstraction and the O–H bond being made in the iron–hydroxo complex of the $^{4,2}C_I$ intermediates in Figure 1. Since BDE$_{OH}$ is a constant value throughout the series of H-abstraction reactions discussed in this work, and the interaction energies of the radical with the iron–hydroxo are small and virtually constant,[37a] this implies that the variation in the reaction energy will depend on the BDE$_{CH}$ quantity only.

Figure 4a shows the correlation of the averaged doublet and quartet spin state barriers vis-à-vis the corresponding BDE$_{CH}$ (correlations for the individual spin-state barriers are shown in Figures S13–S20 of the Supporting Information). It is seen that the correlation is relatively poor, with a correlation coefficient of 0.64. Figure 4b shows the corresponding correlation with the bond strength quantity, D_{CH} (eq 3). This correlation is much better, thus indicating that the strength of the interaction in the C–H bond has to be considered rather than merely the BDE$_{CH}$ that dominates the thermodynamic driving force. Many other correlations, shown in the Supporting Information, for example, the barrier height with ZPE correction, lead to the same
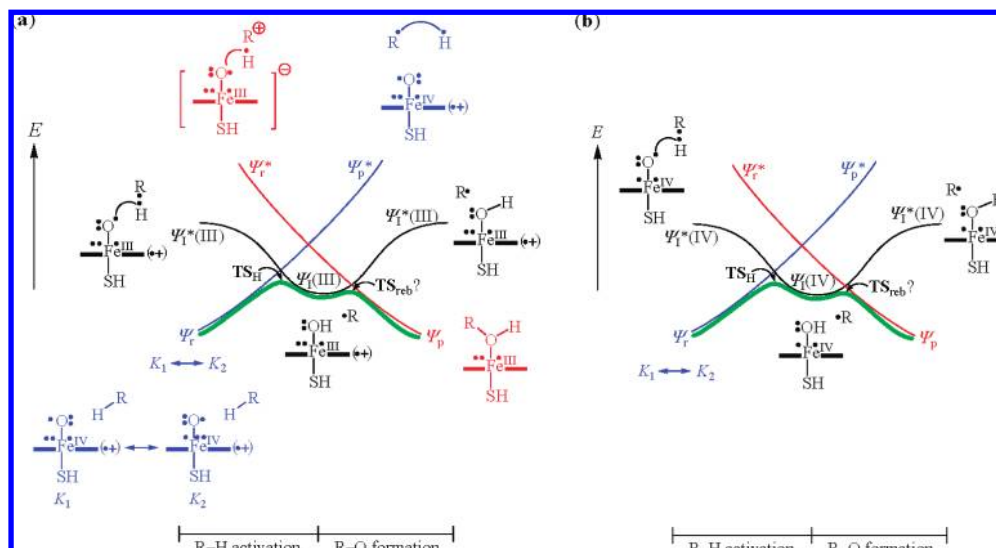
Figure 5. VB diagrams describing the mechanisms of C—H hydroxylation of an alkane (R—H) by Cpd I (the porphyrin is symbolized by the two bold lines flanking the iron) for two electromeric states: (a) formation of the Por$^{+\bullet}$Fe^{III}OH/R$\bullet$ intermediate, and (b) formation of the PorFe^{IV}OH/R$\bullet$ intermediate. The diagrams can represent either quartet or doublet spin states. The spin pairing in the excited state is indicated by a curved line connecting electrons on two different atoms.[20b] The reactant curve with its relevant structures is shown in blue and the product curve in red. The bold green profile shows the state curve during the reaction process.

conclusion. The D_{CH} values of **6** and **9** deviated significantly from the line due to underestimated RE values in comparison with our previous studies and have been omitted from the correlation.[8b] These deviations will be explained during the VB modeling.

Discussion

The above results show some interesting patterns that require understanding: First, why is the entire hydroxylation process stepwise, with H-abstraction and rebound steps, and not a concerted oxygen atom transfer? Second, what factors govern the barriers for H-abstraction in a fundamental manner that does not rely on correlations? Then there is a host of related questions: What is the source of the polar effect, which is apparent from the charge transfer data in Figure 2? Finally, what factors govern the barrier for the rebound? In order to achieve the requisite insight, we shall use the VB approach to model the mechanism and the origins of the various barriers.[20] In the end, we shall show that the barriers can be calculated from raw data based on the VB state correlation diagram (VBSCD) model.[39]

Modeling the Mechanism of C—H Hydroxylation Using Valence Bond Diagrams. As we already noted, there are two electromeric intermediates[36] that may be involved during the reactions: Por$^{+\bullet}$Fe^{III}OH and PorFe^{IV}OH species. In addition, there are two spin states, with doublet and quartet spins, which lead to distinct reaction profiles.[32] In order to economize the discussion, we shall model the mechanisms for the two electromeric states and comment on the spin-state effect only by reference to the rebound step.[37a]

Figure 5 shows the VB diagrams for the hydroxylation reactions involving the two electromeric intermediates; the alkane is symbolized as R—H and the porphyrin ring by the bold lines flanking the iron. The two diagrams involve two major curves that correspond to reactants and products states shown in blue and red, respectively. A third curve that cuts through the high-energy ridge of the other two major curves provides a

(39) Su, P.; Song, L.; Wu, W.; Hiberty, P. C.; Shaik, S. *J. Am. Chem. Soc.* **2004**, *126*, 13539–13549.

low-energy pathway for the transformation.[20b] Looking at the wave functions of reactants and products, labeled as Ψ_r and Ψ_p at the lower two ends of each diagram, it is seen that the overall process of conversion of the alkane, R—H, to an alcohol involves also a two-electron reduction of iron—oxo porphyrin, which changes from Por$^{+\bullet}$Fe^{IV}=O to PorFe^{III}(alcohol). This, however, is mediated by the intermediate curve that describes a H-abstraction process, whereby the electron of the abstracted H$\bullet$ reduces either the oxidation state on iron to Fe^{III} (Figure 5a) or the oxidation state of the porphyrin from a cation-radical to a closed-shell species (Figure 5b). This step is followed by radical rebound, where an electron shift from the alkyl radical (R$\bullet$) to the iron—porphyrin moiety generates the alcohol and the ferric—porphyrin, which is twice-reduced vis-à-vis the reactants state. *This three-curve VB diagram is a typical case, where an intermediate state internally facilitates the otherwise more difficult transformation of Ψ_r directly to Ψ_p.*

To facilitate understanding of the state correlation in the VB diagram, we have to digress and translate the VB representation of the various anchor states [Ψ_r, Ψ_r^*, Ψ_p, Ψ_p^*, Ψ_I^*(III), and Ψ_I^*(IV)] to the more commonly used molecular orbital (MO) diagram and the language of oxidation state formalism.[32,37] The two major curves describe the transformation of reactants to products and are anchored in two ground states, Ψ_r and Ψ_p, for the reactants and products and two corresponding excited states, Ψ_r^* and Ψ_p^*. Each state-curve represents a single bonding scheme: Thus, Ψ_r describes the bonding pattern in the reactants, and so does Ψ_p^*, only that the latter state represents the reactant-type bonding in the geometry of the products. Similarly, Ψ_r^* involves the product-type bonding but in the geometry of the reactants. As a result of these bonding features, as we move along the reaction coordinate, by stretching the C—H bond and shrinking the O—H and R—O distances and thereby changing the geometry from reactants to products, the Ψ_r state connects to Ψ_p^* and, at the same time, Ψ_r^* connects to Ψ_p. Let us now inspect these four states in terms of electronic structure cartoons in detail.

Scheme 3. Electronic Structure of Cpd I: (a) VB Representation[a] and (b) MO Representation
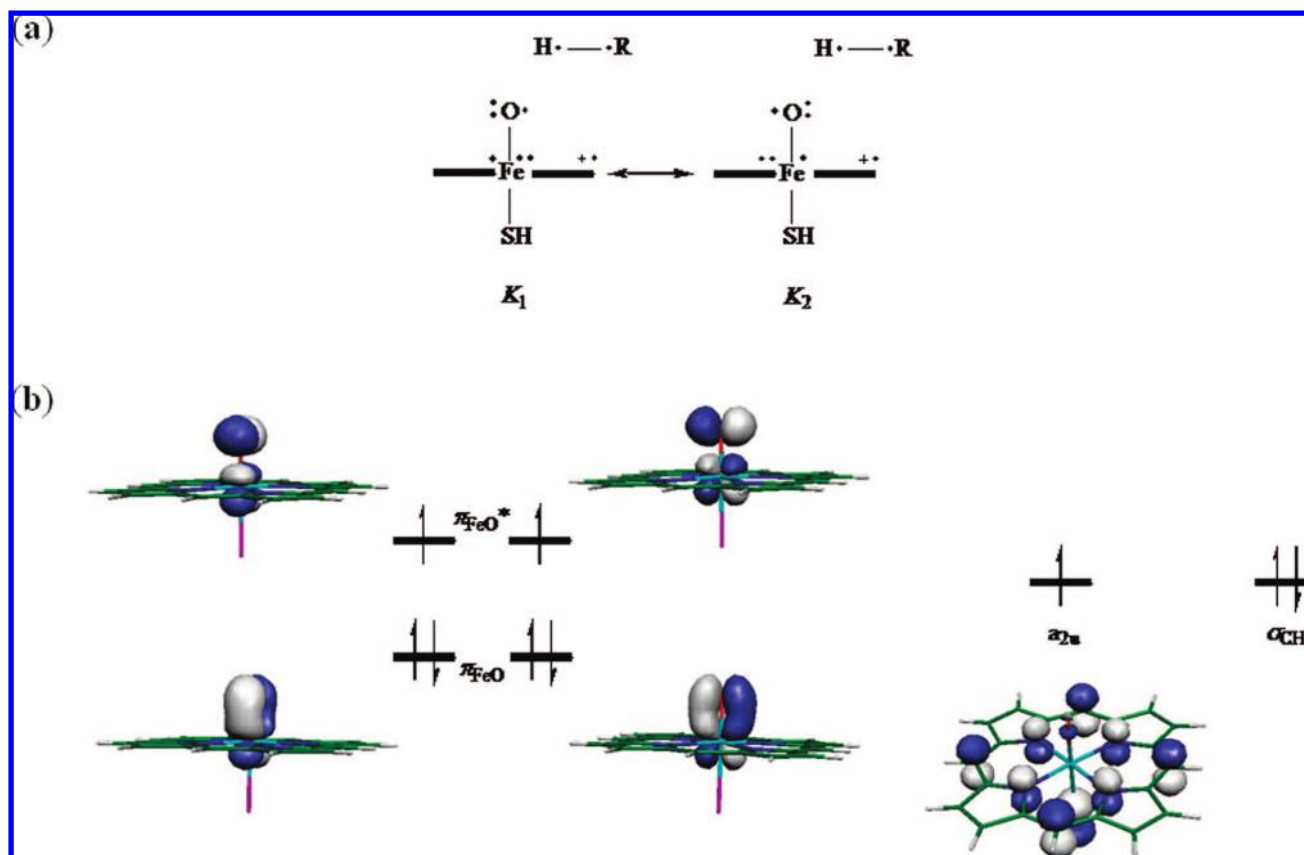
[a] Here the dots on both sides of Fe represent the π-electrons in two perpendicular planes, and the Fe–O line represents the σ-bond.

Starting with the reactants state, Ψ_r (Figure 5), we depict in Scheme 3 the VB-MO representation of Ψ_r for ^{4}Cpd I and R–H. In the VB formulation (Scheme 3a), Cpd I has six π-electrons, distributed in two perpendicular planes, across the Fe–O moiety, and are coupled to produce a triplet spin state.[40] This is described by a resonance mixture of the two forms (K_1 and K_2) that lead to formation of two three-electron bonds in the two perpendicular planes; the line connecting the Fe and O atoms in Figure 5 and here in Scheme 3 represents the σ-bond. The porphyrin is open shell, as indicated with a cation–radical sign. In the MO formulation (Scheme 3b) these six π-electrons on the FeO moiety occupy two bonding π_{FeO} orbitals and two singly occupied antibonding π^*_{FeO} orbitals.[32] The third unpaired electron of Cpd I resides on the porphyrin in an a_{2u} type orbital, and its spin is either ferromagnetically or antiferromagnetically coupled to the triplet FeO pair, thereby yielding two spin states: overall quartet or doublet. In addition, there are three more orbitals originating from the 3d metal atomic orbitals, namely one doubly occupied d(δ) orbital on iron and two virtual antibonding orbitals (σ^*_{xy} and $\sigma^*_{z^2}$), which are not shown explicitly in Scheme 3. The alkane R–H is represented in VB by the corresponding Lewis structure and in MO in terms of the bond orbital σ_{CH} of the R–H bond undergoing activation.

The excited state Ψ_r^* in Figure 5 is a charge transfer state in which one electron is transferred from the R–H alkane to fill the "hole" in the a_{2u} orbital of the porphyrin radical cation of Cpd I, while at the same time the H• moiety is spin-paired to

the odd electron on the oxo group. This spin-pairing[41] is shown in Figure 5a by the curved line connecting the single electrons on H• and on the oxo group of Cpd I; the RH moiety in this state is a cation–radical. With these bonding changes, the oxidation state of iron in Ψ_r^* is reduced from Fe^{IV} to Fe^{III}. The assignment of oxidation state for Ψ_r^* is based on an electron counting formalism, which needs a brief explanation. Thus, in Ψ_r, the oxo group of Cpd I is counted as O^{2-}, the four nitrogen ligands of the porphyrin as N$_4^{2-}$, and the sulfur of the cysteine as S^{1-}. Since Cpd I is neutral, these oxidation states require the iron to be Fe^{IV} and the porphyrin a cation–radical species. However, in Ψ_r^*, the oxo is spin-paired to H•, and as an "OH" group its oxidation state becomes HO^{1-}, so the iron ion changes to oxidation state Fe^{III}. Thus, by linking the H• atom to the iron–oxo, the oxo group accepts formally one electron from the H-atom, and hence it "releases" back one of the two electrons it took from Fe in Cpd I. This, in addition to the actual charge transfer from R–H to the heme Ψ_r^*, makes this state "twice reduced" relative to the reactant state, Ψ_r. As such, along the reaction coordinate, which involves R–H bond elongation and O–H and O–R shortening, the Ψ_r^* state gets stabilized by forming O–H and O–R bonds and becomes the ground state of the ferric–alcohol product, Ψ_p, which involves three electrons in iron d$_\pi$ orbitals (drawn as heavy dots on iron). Thus, Ψ_r^* is the electronic image state of Ψ_p and hence the two states correlate along the reaction coordinate. The same applies in fact to the relationship between the states Ψ_r and Ψ_p^*; the latter being the electronic image of the former, with spin-pairing

(40) Shaik, S.; Danovich, D.; Fiedler, A.; Schröder, D.; Schwarz, H. *Helv. Chim. Acta* **1995**, *78*, 1393–1407.

(41) Shaik, S.; Hiberty, P. C. *A Chemist's Guide to Valence Bond Theory*; Wiley-Interscience: New York, 2007; see, in particular, Chapter 3.
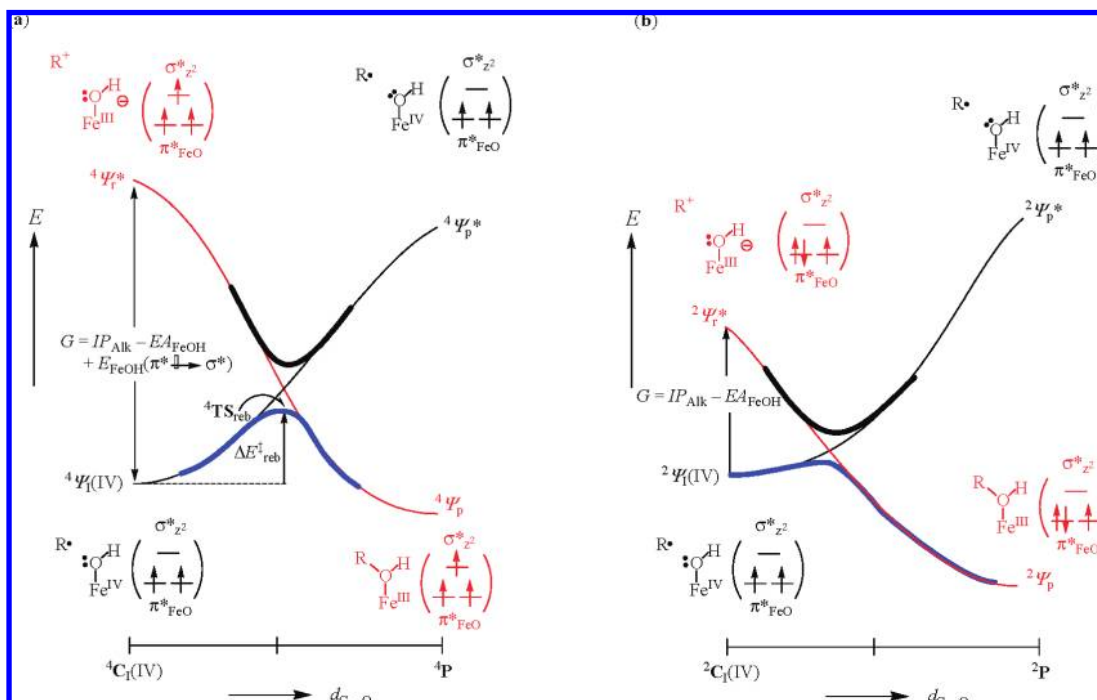
Figure 6. VB mixing and avoided crossing during the rebound processes of the quartet (a) and doublet (b) spin states of the PorFe^{IV}OH/R• intermediate.

between R and H, but with the geometry of the product. As such, the two states correlate with one another along the reaction coordinate.

Let us turn now to the intermediate curves, which are labeled as Ψ_I*(III) in Figure 5a and Ψ_I*(IV) in Figure 5b. In the VB representation, the C–H bond in R–H is unpaired into a triplet spin,[20b,39] and the H• atom is spin-paired to the odd electron on the oxo group. As already discussed above, this spin-pairing changes the oxidation state of the OH moiety to −1 and "releases" one electron to the heme. In the case of Ψ_I*(III), this electron is given to iron, which is reduced to Fe^{III}, while in Ψ_I*(IV), the electron shifts from the iron into the porphyrin hole and the iron keeps two unpaired electrons in the dπ orbitals, thereby remaining in oxidation state Fe^{IV}. In each case, the entire intermediate curve corresponds to a single VB structure but in different geometries. Thus, at the intermediate stage, it corresponds to an H-abstraction intermediate (C$_I$ in Figure 1), composed of an iron–hydroxo/R• species, where the iron–porphyrin is in two electromeric states (Por$^{•+}$Fe^{III}OH or PorFe^{IV}OH). Similarly, at the product geometry, this state involves a charge transfer from porphyrin to the R–O linkage in Figure 5a, or from the iron d-electrons to the same linkage in Figure 5b.

The final energy profile for the mechanism in Figure 5 involves VB mixing of the three curves. The mixing that is shown by the bold green lines leads to avoidance of the crossing and generates the corresponding transition states, initially, for the H-abstraction step, TS$_H$, and subsequently for the radical rebound via TS$_{reb}$. The latter transition state exists only on the quartet energy profile (see analysis below), as has already been rationalized using VB diagrams.[37] To denote the spin-state condition on the existence of this particular barrier, we marked the symbol TS$_{reb}$ in Figure 5 with a question mark.

The polar character of the TS$_H$ species, defined above in Figure 2 as the degree of charge transfer, Q_{CT}, arises from the secondary VB mixing of the Ψ_r* curve into TS$_H$. All these features are apparent in the computational results discussed

above by reference to Figures 1 and 2 and analogous findings summarized in papers and reviews.[31,32,37] Furthermore, it is seen from Figure 5 that the intermediate curve catalyzes the two-electron oxidation process by cutting through the high barrier, which would have been encountered otherwise due to the crossing of the main curves that emanate from reactants and products, Ψ_r and Ψ_p. Therefore, in addition to revealing the source of the polar effect (see Q_{CT} in Figure 2), the VB diagram accounts nicely and simply for the findings, both experimentally,[15] and computationally,[32,37] of a stepwise rather than a concerted process. Additionally, the geometric characteristics of the H-abstraction transition states, and the correlations of %BB and %BF with the corresponding energy barriers (see Figure 3), reflect the mechanism of an avoided crossing that leads to the transition states. Thus, the crossing of the reactant (Ψ_r) and intermediate [Ψ_I*(III)] curves, to establish TS$_H$, is caused by C–H stretching and O–H approach, and hence, the barrier correlates with the progress of these geometric features compared with the reactants state.

Let us discuss the spin-state effect on the rebound process.[37] The VB diagram for the rebound step on the two spin states of the PorFe^{IV}OH/R• electromer is shown in Figure 6. This figure starts from the center of Figure 5b, where the intermediate curve Ψ_I(IV) has to cross the Ψ_r* curve that descends toward the product state Ψ_p. To clarify the argument, we show compact MO occupation diagrams in Figure 6 describing the three upper MOs of the d-block. Figure 6a shows the situation for the quartet spin state, while the doublet spin curve is depicted in part b. At the intermediate geometry, the Ψ_r* state includes an electron transfer from the radical moiety R• to the iron–hydroxo complex. To maintain a quartet-spin, the electron is transferred into the high-lying σ*$_{z^2}$ orbital, while for the doublet state in Figure 6b the electron is transferred into a lower-lying π* orbital. The height of the crossing point depends on the initial gap between the two curves: the larger this gap, the higher the crossing point. Consequently, in the quartet spin state, where

the gap is large (the difference is 26 kcal mol^{-1}),[37a] the VB mixing will generate a barrier for rebound. On the other hand, in the doublet spin state the gap is much smaller (by 26 kcal mol^{-1}) so that the avoided crossing yields a barrier-free radical rebound. This trend has been observed so far in all the calculations done by our groups.[31,32,37] An explanation why the quartet rebound barrier is significantly higher for the $^4\Psi_I$(III) electromer compared with the $^4\Psi_I$(IV) electromer has been given before in VB terms and will not be repeated here.[35,37]

All in all, the VB diagram model provides a good rationale for the computational and experimental findings on various aspects of P450 hydroxylation. Let us turn now to a more quantitative aspect of the modeling.

Modeling of the Barriers for H-Abstraction Using the Valence Bond Diagram. Figure 7 shows the VB diagram for only the first step in the reaction mechanism, namely the one representing the C−H bond activation. The two curves (Ψ_r and Ψ_I*) are initially separated by an energy gap G_H (the so-called promotion gap[20b,41]) and cross one another along the reaction coordinate to generate a transition state (TS$_H$) through VB mixing and avoidance of the crossing.

The barrier for the reaction, $\Delta E^\ddagger$ can be expressed as the height of the crossing point, ΔE_c, minus the resonance energy (B) of TS$_H$ due to the VB mixing:

$$\Delta E^\ddagger = \Delta E_c - B \qquad (5)$$

The height of the crossing point in turn can be expressed as a fraction (f) of the promotion gap (G_H):

$$\Delta E_c = f G_H \qquad (6)$$

Combining these two equations, an expression for the barrier heights is derived:

$$\Delta E^\ddagger = f G_H - B \qquad (7)$$

This effective equation includes the BBEP effect of the reaction driving force directly into the f factor and is the most convenient one to use.[42]

On the basis of previous modeling of the barrier for H-abstraction process, we have established[39] that f is approximately 0.3, while B is given by eq 8:

$$B = \frac{1}{2} \text{BDE}_W \qquad (8)$$

Here BDE$_W$ stands for the bond dissociation energy of the weakest bond among the two that are formed and broken during the reaction: either the C−H or FeO−H bond. Restricting ourselves to the highest level calculations (with basis set B2), all the BDE$_{CH}$ values in our series (1−10), except those for propene (**4**), *trans*-isopropylphenylcyclopropane (**6**), *N,N*-dimethylaniline (**7**), toluene (**8**), and phenylethane (**9**), are larger than BDE$_{OH}$. Thus, B can be estimated from the raw data of BDEs tabulated in the Supporting Information and in Table 2.

(42) See Chapter 6 in ref 41. Using the gaps and f factors on both sides of the diagram, one obtains an equation that involves explicitly the effect of the driving force on the barriers. However, this equation requires knowledge of the two gaps and individual f factors and is therefore less convenient to use.

(43) The G value for the Fe^{IV} electromer includes also the promotion energy of an electron from π^*_{FeO} to the a_{2u} orbital. This is a constant quantity, previously evaluated to be ~5−6 kcal mol^{-1}. See: Ogliaro, F.; de Visser, S. P.; Groves, J. T.; Shaik, S. *Angew. Chem. Int. Ed* **2001**, *40*, 2874−2878.
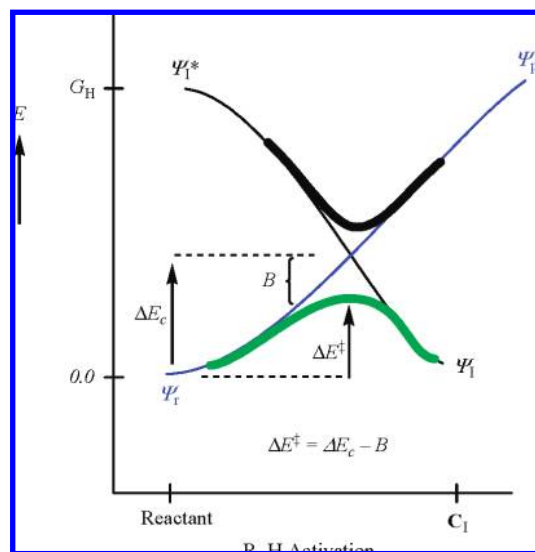
Figure 7. VB diagram showing the barrier formation for the H-abstraction step and the factors controlling its height.

Finally, the promotion gap G_H was shown[20b,39,41] to involve ca. 75% of the corresponding singlet-to-triplet promotion of the C−H bond that undergoes activation[43] and to be given to a good approximation by eq 9 as twice the bond strength of the activated C−H bond:

$$G_H = 2D_{CH} = 2(\text{BDE}_{CH} + \text{RE}_{Alk}) \qquad (9)$$

Using the data in Table 2, we can quantify all the corresponding G_H factors.

Thus, in principle, all the quantities necessary for calculating the barriers for C−H activation from raw fundamental data are available. However, it would be more interesting to show that the barriers themselves produce the proposed values of $f \sim 0.3$ and B values (eq 8). There are two ways to do so: in one, we use eqs 7−9 and find the f values that reproduce the calculated barriers, while in the second, using eqs 7 and 9 with $f = 0.3$ for all the reactions we find the corresponding B values that are required to produce the barriers. Subsequently, we shall compare the so obtained f and B quantities to the values proposed above from previous theoretical modeling.[39] To economize the data, we model only the highest level barriers at B2 averaged over the doublet and quartet spin states. The data are collected in Table 3 along with the calculated B2 barriers in the first column.

In the first method of modeling, we used the B values according to eq 8 and found the f values that would be required to reproduce the computed barrier. For all the substrates except for **4**, **6**, **7**, **8**, and **9**, the weakest bond is FeO−H, giving $B = 44.45$ kcal mol^{-1}, whereas for the other substrates, the weakest bond is C−H, leading to $B < 44.45$ kcal mol^{-1}. Using these values and G_H according to eq 9, the so obtained f values gave an average value of $f_{av} = 0.285 \pm 0.015$; i.e., they all cluster around the theoretical value of 0.3. The barrier data in the second column shows the barriers computed with eq 7 and $f_{av} = 0.285$. The so reproduced barriers are close to the B3LYP/B2 computed ones within a scatter of ± 2.4 kcal mol^{-1}.

In the second method of modeling, we use $f = 0.3$ and find those B values that reproduce the barriers. That way, the values cluster around an average $B_{av} = 46.39$ kcal mol^{-1} with a scatter of ± 2.24 kcal mol^{-1}. The largest deviations are for the substrates **1** and **7**, for which the B values are 3.97 kcal mol^{-1} smaller and 4.76 kcal mol^{-1} larger than the average quantity. The same
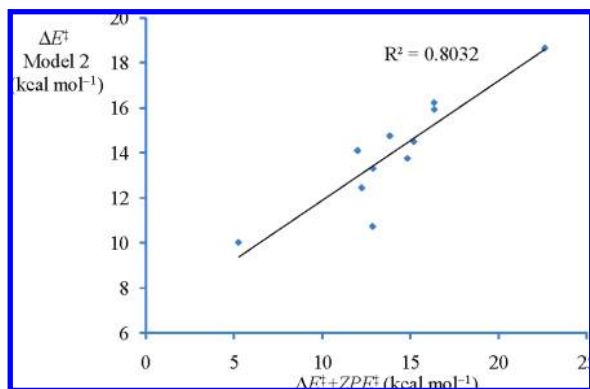
Figure 8. A plot of the VB barriers (last column in Table 3) against the DFT calculated barrier heights.

two substrates also deviate in the first method. With these two substrates excluded, the estimated barrier heights (column 3 in Table 3) show a deviation of ± 1.80 kcal mol^{-1} from the DFT calculated values. We shall account for these deviations later.

The last column of Table 3 collects the barriers obtained with eq 7 using $f = 0.3$ and $B_{av} = 46.39$ kcal mol^{-1}. These barriers are close to the computed ones with a scatter of ± 1.53 kcal mol^{-1}, which improves to ± 0.90 kcal mol^{-1} when the outliers for methane and N,N-dimethylaniline are removed from the data set. The two deviations have clear physical origins, which are explained in the following sections. Just to provide a pictorial representation, we show in Figure 8 a plot of the so estimated VB barrier vis-à-vis the DFT calculated values; the correlation is reasonably good. We may therefore conclude that the VB models can predict barrier heights quite well of P450-catalyzed reactions in the gas phase.

It is important to comment here on the relationship of the VB model to the often used BBEP correlation with the BDE$_{CH}$ quantity. Thus, while eq 9 shows that the gap in the VB diagram (Figure 7) is related to BDE$_{CH}$, it also shows that this relation does not derive from the BBEP principle.[12] The actual correlation is between the barrier and the promotion gap that originates it. Thus, the correlation per se cannot invoke causality unless one reveals the mechanism of the correlation, as done, for example, in the VB diagram.

Barriers for H-Abstraction for the Fe^{IV} vs Fe^{III} Electromeric State. Thus, while the values of G_H in both cases are virtually the same,[43] the two states $^4\Psi_I^*(IV)$ and $^4\Psi_I^*(III)$, which cross $^4\Psi_r$ or generate the corresponding intermediate, are different and their energy descent is different as well. In Figure 5b, the state, $\Psi_I^*(IV)$, that crosses Ψ_r down to the PorFe^{IV}OH/R• intermediate has an odd electron that is localized on the oxo group. By contrast, $\Psi_I^*(III)$ in Figure 5a has two resonance structures that delocalize the odd electron on the oxo group between two planes. Therefore, the bond coupling interaction of the spin-paired moieties, H•−•O, in $\Psi_I^*(IV)$ is strong, while in $\Psi_I^*(III)$ the same interaction is weaker. The result is that $\Psi_I^*(IV)$ establishes a low-energy crossing point (smaller f in eq 7), while $\Psi_I^*(III)$ establishes a higher crossing point (larger f in eq 7). Consequently, the barrier for the Fe^{III} electromer will be generally higher than the one for the Fe^{IV} electromer. Furthermore, this higher barrier is expected to be attended by TS$_H$(III) species that lie later on the H-transfer coordinate, having greater extents of elongations of the R−H and Fe−O bonds than the corresponding TS$_H$(IV) species. An example for an TS$_H$(III) species is the case of methane (**1**) activation, where the spin density distribution (in Tables S5 and

S6 of the Supporting Information) clearly shows that it has Fe^{III}Por$^{+\bullet}$ character. Figure 2 shows that indeed the C−H bond is extensively cleaved in the TS, being 1.489 (1.499) Å. The strength of the C−H bond in methane being the largest in the series requires extensive bond stretching to achieve the TS. With such a TS geometry, the lowest electromer is of the Fe^{III}Por$^{+\bullet}$ variety and the transition states are ^{4,2}TS$_H$(III) types. This in turn means that a larger f value is required in the VB model to reproduce more accurately the corresponding barrier for methane hydroxylation, and this is the reason why use of $f = 0.3$ underestimates the barrier in Table 3.

However, notwithstanding methane, in the gas phase we seldom expect to find the TS$_H$(III) species being lower than the TS$_H$(IV) species. The same applies to the corresponding intermediates, where invariably the lowest state is for the PorFe^{IV}OH/R• electromer. However, the Fe^{III} electromers, which possess a porphyrin cation−radical moiety, are more polarizable compared with the Fe^{IV} electromers.[36] Consequently, in a strongly polarizing medium like the protein, the Fe^{III} electromeric states are stabilized compared with the Fe^{IV} states and generally become the lower energy species. All the QM/MM calculations show these trends.[37,38] Indeed, the TS geometries in the protein show larger extents of C−H stretching and greater O−O formation than the corresponding gas-phase species. Camphor (**10**) is a case in point, where the QM/MM-optimized transition state species are of the ^{4,2}TS$_H$(III) variety and their C−H bonds are longer compared with the corresponding gas-phase species.[38a]

Polar Effects in P450 Hydroxylation−The Case of N,N-Dimethylaniline (7). We recall that the C−H bond activation barrier for this substrate is very small and it deviates from the VB barriers of the other substrates. Inspection of Table 2 shows that the BDE$_{CH}$ of **7** is much like that in toluene (**8**), but the corresponding barrier is 7−8 kcal mol^{-1} lower! The reason for this is a strong polar effect in the corresponding TS$_H$ species.[14b,c] The polar effect is apparent from the amount of charge transfer, Q_{CT}, which is close to 0.5, which indicates a very strong mixing of the radical−cation state into the TS$_H$ species (see Ψ_r^* in Figure 5). This mixing is enhanced by the conjugation between the lone pair and the empty orbital on carbon in the N−CH$_2^+$. In fact, the extensive lone pair conjugation in the TS$_H$ species can be deduced also by inspecting the amount of radical development on the nitrogen atom in TS$_H$ of **7** in Scheme 4. It

Table 3. B3LYP/B2//B1 Barriers (kcal mol^{-1}) [$\Delta E^{\ddagger}$(DFT)] and Barriers Modeled by VB Theory [$\Delta E^{\ddagger}$(VB)]

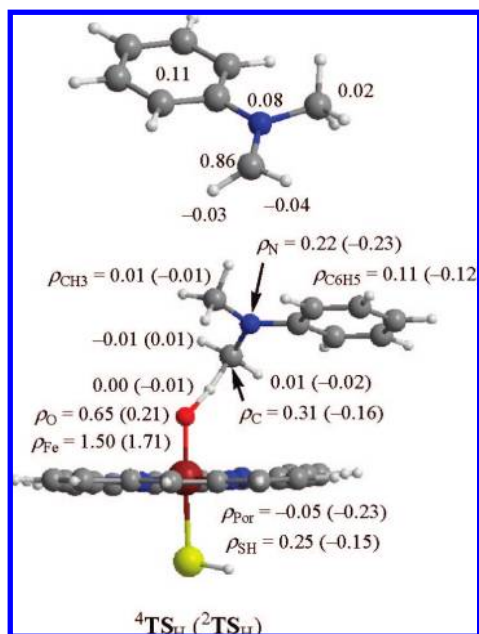| system	$\Delta E^{\ddagger}$(DFT)	$\Delta E^{\ddagger}$(VB) model 1[a]	$\Delta E^{\ddagger}$(VB) model 2[b]
1	22.63	17.41	18.66
2	16.35	14.82	15.93
3i	14.82	12.75	13.75
3n	16.34	15.10	16.23
4	12.89	15.38	13.31
5	13.83	13.71	14.76
6	12.86	11.03	10.73
7	5.27	10.61	10.02
8	12.24	13.07	12.45
9	12.01	16.31	14.10
10	15.20	13.47	14.51

[a] Use of eq 7 leads to $f = 0.285 \pm 0.015$. All the barriers were calculated with eq 7 as follows: $\Delta E^{\ddagger}$(VB) $= 0.285\,G_H - B$; $B = 44.45$ kcal mol^{-1} (0.5 BDE$_{OH}$) with the exception of **4**, **6**, **7**, **8**, and **9**. [b] Use of eq 7 and $f = 0.3$ leads to $B_{AV} = 46.39 \pm 2.24$ kcal mol^{-1}. The barriers were calculated using eq 7 as follows: $\Delta E^{\ddagger}$(VB) $= 0.3\,G_H - B_{AV}$.

can be seen that the nitrogen develops spin density in the TS$_H$ species to an extent larger than in the isolated radical species *N*-methyl-*N*-methylenylaniline radical. This enhanced conjugation increases the resonance energy of the transition state[14c] and thereby lowers the barrier. Thus, the deviation of **7** in Table 3 is caused by the *B* factor that gets larger (compared with eq 8) due to the enhanced conjugation of the nitrogen lone pair in the transition state. Indeed, as shown recently by Wang et al.,[14b] the H-abstraction barriers in a series of para-substituted *N,N*-dimethylaniline derivatives exhibit a Hammett correlation that reflects the substituent effect due to the ability of the nitrogen lone pair to conjugate with the stretched C−H bond in the TS.

Conclusions

Density functional theoretic studies on a series of hydrogen abstraction barriers of cytochrome P450 reactions show that the barriers correlate linearly with the bond strength (D_{CH}) of the C−H bond that is broken, rather than with the corresponding bond dissociation energy (BDE$_{CH}$). Structurally, the trends show that high barriers are associated with product-type TS geometries with long C−H bonds and short O−H bonds, while the low-barrier processes have reactant-type structures. These structural and energetic trends of hydrogen-bond energies are accounted for by the valence bond model of chemical reactivity.[20] The model shows that the correlation between the barrier and the corresponding D_{CH} quantities is the promotion energy gap (G_H, Figure 6) that has to be overcome by molecular distortions in order to establish the transition state. Using these promotion gaps, the valence bond model can predict quantitatively the barriers with reasonable reproducibility. The model explains other features of P450 hydroxylations as well: (a) the nature of the polar effect, (b) the difference between the activation mechanisms leading to the Fe^{IV} vs the Fe^{III} electromers, (c) the difference between the gas phase and enzymatic reaction, and (d) the dependence of the rebound barrier on the spin state.

The valence bond mechanism in Figure 5 shows that compound I can perform a complex reaction that involves multiple bond making−breakage by utilizing an intermediate valence bond structure that cuts through the high barrier of the principal transformation between reactions and products, thereby mediating the process at a lower energy cost (Figure 5). The correlations derived in this paper, along with previous treatment of the rebound process,[37] create order and organize the data for a process of a complex and important enzyme. While this treatment has obvious bearing also on the reactivity patterns in the nonheme systems,[2] a straightforward extrapolation is not possible due to the existence of triplet and quintet spin state surfaces with different barrier heights.[44] A preliminary VB model for C−H activation by nonheme reagents was described in ref 23b.

Supporting Information Available: Detailed comparison of Jaguar- and Gaussian-optimized geometries, Cartesian coordinates of all structures described in this work, tables with group spin densities and charges, figures with various correlations, as well as complete refs 22 and 24. This material is available free of charge via the Internet at http://pubs.acs.org.

(44) (a) Hirao, H., Jr.; Nam, W.; Shaik, S. *Chem. Eur. J.* **2008**, *14*, 1740–1756. (b) de Visser, S. P. *J. Am. Chem. Soc.* **2006**, *128*, 15809–15818.